 doi:10.20944/preprints202208.0361.v1

Article

Design and Characterizing of Blower Wind Tunnel Using CFD

Itimad D. J. AZZAWI

Faculty of Engineering, University of Diyala, Diyala, Iraq
Correspondence: Itimaddawood_eng@uodiyala.edu.iq

ABSTRACT

A new subsonic blower wind tunnel design has been studied both numerically and experimentally, it is also referred to as "blower" wind tunnel. This paper, is initially aimed to address each sequential stage of the wind tunnel design process. Rather than applying the standard method of modelling solely the flow in the test section, a large-scale CFD model of the whole wind tunnel was employed. The loss of every constituent element was calculated and then all the losses are added up to determine the power needed for the wind tunnel operation which is used as "intake fan" boundary conditions in the CFD model. Then, flow uniformity and turbulent intensity measurements in an empty test section using a Pitot-static tube and hot wire anemometer (HWA) were introduced to validate the CFD results. The results showed that flow quality was significantly affected by boundary layer controllers (honeycomb and mesh screens) in the settling chamber and wide-angle diffuser. Investigations were also conducted to evaluate the flow deficit in the wake area behind a convex hump model using HWA. This was additional experimental tests carried out to validate the suitability of the wind tunnel flow aerodynamic research.

Keywords: Blower wind tunnel design; CFD; Boundary layer controller; Turbulent intensity; Validation; Power spectral density (PSD)

1. INTRODUCTION

Wind tunnels of small size are increasingly being employed in aerodynamic studies to explore the behaviour of airflow over solid objects such as airfoils and cylinders which are becoming increasingly popular in aerodynamic research. It produces a flow characterised by relative steadiness, homogeneity, and low turbulent intensity within the test section. The purpose of wind tunnel experiments is to aid the determination of flow behaviour over aerodynamic objects, which is required in the design process of such objects. Thus, in order to ensure the precision of

 doi:10.20944/preprints202208.0361.v1

measurements in the wind tunnel and the similarity of test section conditions to real atmospheric conditions, the wind tunnel need be designed and produced efficiently. However, despite the applicability of wind tunnels, there are constraints in terms of their cost, size and limited understanding of their design **[1].**

These two distinct types of wind tunnels include closed-circuit and open-circuit. In the case of the open-circuit type, the test section can be either closed or open. There are several reasons that justify the selection of the open-circuit type. First of all, in case of investigating a large scale of models, for which a large test section is required to avoid the occurrence of blockage, the open-circuit wind tunnel is fulfilled this condition, as it supplies more space in which the airflow can move around the model. The second reason is that, for the purposes of this research, an open-circuit wind tunnel is more cost-efficient than the closed-circuit type, providing an identical desired wind speed and flow area. Finally, the open-circuit wind tunnel is easier to use in a confined laboratory environment. However, it has been found that open-circuit tunnels with centrifugal blower at the entry are much less sensitive to disturbances in the entry flow than suction tunnels. Some of the first blower tunnels designed include Clauser's boundary layer tunnel (1954) and the Liverpool University 4' × 2' (1959), although the latter had an axial fan.

An atypical wind tunnel consists of a standard structure including the contraction, test section and diffuser. The contraction component significantly increases airflow velocity prior to entering the test section; wind tunnels generally should have contraction ratios of 6-9 **[2]**. The test section houses the test object during the study and typically, the test object dictates the size of the test section. A wide-angle diffuser in a blower wind tunnel needs to be designed carefully to reduce the flow separation in the corners.

The standard condition specifies that the flow of the test section should display stability, uniformity, and low turbulent intensity, which indicated the flow quality inside the wind tunnel. Efficient devices of boundary layer controller in the settling chamber such as honeycomb and mesh screens with a suitable ratio of contraction area are the typical factors causing the freestream velocity in the test section to be uniform with low-turbulent intensity. Furthermore, extensive separation in

 doi:10.20944/preprints202208.0361.v1

upstream elements like the diffuser also makes the freestream velocity in the test section unstable with high turbulent intensity.

However, it is difficult and unwise to predict fixed rules for wind tunnel design. This is mainly due to the wide variety of tunnel designs and the lack of understanding of flow through wind tunnel components such as the diffuser, screens and the blower itself. Therefore, the development of an open-circuit blower wind tunnel is described in this paper. Pressure losses were first determined for each component, before being combined to ensure that the loss of each integral element was computed; thus, the complete pressure loss of the whole circuit was ascertained. Computational fluid dynamics (CFD) and experimental evaluation was then implemented in order to compare airflow characteristics through the wind tunnel test section. Assessments were finally carried out to evaluate the wake flow behind a "convex" hump model using HWA and PIV. These supplementary studies were performed in order to determine the adequacy of the wind tunnel flow in future aerodynamic studies.

2. PREVIOUS LITERATURE RELATED

Fluid flow and heat transfer in configurations of great complexity can be modeled with the advanced computer software FLUENT. The main advantage of this software is that it affords extensive mesh flexibility and facilitates flow problem resolution through unstructured meshes, which can be produced easily around complex configurations. The software is compatible with a variety of mesh types, such as two-dimensional triangular and quadrilateral meshes, and three-dimensional tetrahedral, hexahedral, pyramidal, and hybrid meshes. Moreover, FLUENT allows the grid to be refined or broadened in accordance with the flow solution. **Table 1,** outlines an overview of previous studies conducted using CFD to assess open-circuit and closed wind tunnels.

Table 1: Tabulated previous studies of subsonic wind tunnel facilities.

Preprints (www.preprints.org) | NOT PEER-REVIEWED | Posted: 19 August 2022 doi:10.20944/preprints202208.0361.v1

References	Location	Circuit type	Application	Test section (m2)	Speed (m/s)
[3]	Bangkok, Thailand	Open-circuit (Blower)	Fluid-dynamic research	0.6 x 0.18	30
[4]	Gorgia, Atlantic	Open-circuit (Blower)	Turbulent boundary layer studies	0.91 x 1.21	1.8– 12.1
[5]	Stanford, California	Open-circuit (Blower)	Boundary-layer interaction	0.8 x 3	27
[6]	Stanford, California	Open-circuit (Blower)	Turbulent boundary layers studies.	0.762 x 3.748	7
[7]	University of Sheffield, UK	Closed	Fluid-dynamic research	0.5 x 0.5	10
[8]	Sao Paulo, Brazil	Open-circuit	Anemometer calibration	0.5 x 0.5	2-20
University of Leeds	Leeds/ UK	Open-circuit (Blower)	Aerodynamic research	0.5 x 0.5	3-20

3. TECHNICAL REQUIREMENTS FOR THE DESIGNED WIND TUNNEL

The initial stage of the wind tunnel design is the identification of the major components which have been introduced as a design proceeds for each component. In this regard, there are two major conditions were taken in consideration. First, freestream velocity should exhibit variation of up to 20 m/s. Additionally, for a small-scale wind tunnel, the intensity of free-stream turbulence should not exceed 1%. The selection of tunnel type has been weighed carefully in keeping with considerations of functionality, time-efficiency, as well as the possibility to use the design guide from **[1, 2, and 9].** The components and dimensions of the wind tunnel design are summarized in **Figure 1** subsections beginning with the centrifugal fan followed by a wide-angle diffuser, settling

Preprints (www.preprints.org) | NOT PEER-REVIEWED | Posted: 19 August 2022 doi:10.20944/preprints202208.0361.v1

chamber, contraction and ends with the test section. In this regard, the design of each component was presented in **appendix-A**, and the final fabricated design is shown in the next section.

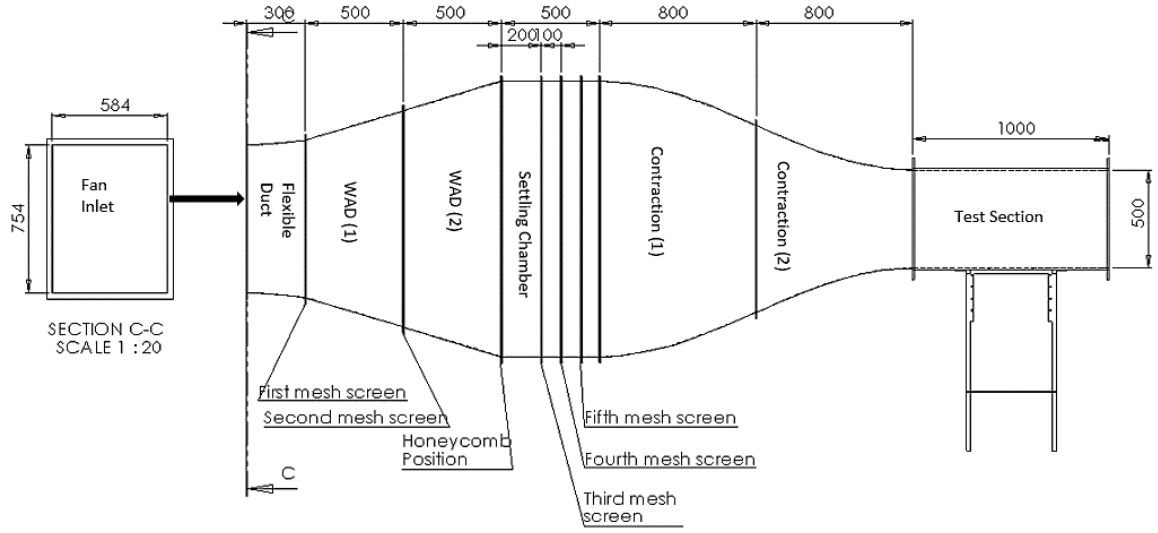

Figure 1: Detailed Solid works model of the open-jet wind tunnel.

4. THE PRESSURE LOSSES OF WIND TUNNEL COMPONENTS

The centrifugal fan drives the wind tunnel by compensating the pressure losses that occurs due to various parts of the wind tunnel. Centrifugal fan rated by the drop of the static pressure that can overcome as well as the volume flow rate that can provide. Consequently, this section presents approaches to the determination of the pressure loss of every wind tunnel element and discusses several fundamental concepts. The method of dividing the wind tunnel into its constituent elements and calculating the losses of individual element was conducted as a way of determining total loss before the numerical simulation.

The purpose of determining the pressure losses of all tunnel elements was to gain an understanding of how the circuit functioned. **Table 2** provides an overview of the total pressure loss coefficients with its formula for both upstream and downstream tunnel components. It can be observed from the table that the wind tunnel had an overall total pressure loss of ~204 Pa including both honeycomb and mesh screens, and this is useful calculation in applying the inlet boundary condition in the CFD analysis.

Preprints (www.preprints.org) | NOT PEER-REVIEWED | Posted: 19 August 2022 doi:10.20944/preprints202208.0361.v1

Table 2: Summary of the design description, pressure formula and loss coefficient of the wind tunnel sections.

Component	Discretion of the component	Pressure formula	Loss coefficient (K)	ΔP (Pa)
Wide-angle diffuser	Wide-angle diffuser area ratio of 3:1 and angle of 16.6° with L = (1 m)	$\Delta Pd = (K_f + K_{ex}) \times 0.5 \times \rho \times V_d^2$ $K_f = \left[1 - \frac{1}{Ar^2}\right][\frac{f}{8 \times sin\theta}]$ $K_{ex} = K_{e(\theta)}(\frac{Ar-1}{Ar})^2$	0.428	25.5
Settling chamber	Square cross-sectional dimensions of 1.4 x 1.4 m2 and length of 0.5 m	$\Delta P = q \times K_s, \quad K_s = \frac{f \times L}{2 \times (R_s)}$	0.0214	1
Contraction	Contraction ratio of 7.84:1, 1.4 x 1.4 m2 (inlet) / 0.5 x 0.5 m2 (exit) length of 1.6 m	$\Delta P = q \times K_n, \quad K_n = 0.32 \times (fav)[\frac{L_n}{D_{ts}}]$	0.01	~1
Test section	Square test cross-section with dimensions of 0.5 x 0.5 m2 and length of 1 m.	$\Delta P = q \times K_{ts}, \quad K_{ts} = \frac{f \times L_{ts}}{2 \times (R_{ts})}$	0.16	61.2
Screens + Honeycomb	Five screens with a porosity of 0.67 and wire diameter of 0.23 mm (dw). One honeycomb with 100 mm thickness and 9.5 mm cell size.	$\Delta P = q \times K_m,$ $K_{m=K_{mesh} \times K_{Rn} \times \sigma_s + \frac{\sigma_s^2}{\beta_s^2}}$ $K_{Rn} = [0.785\left(1 - \frac{R_{ew}}{354}\right) + 1.01]$	5.66	100
Flexible duct		----------	----------	15
Total losses	Total losses include flexible duct			~204

Preprints (www.preprints.org) | NOT PEER-REVIEWED | Posted: 19 August 2022 doi:10.20944/preprints202208.0361.v1

5. NUMERICAL METHODOLOGY AND GOVERNING EQUATIONS.

The actual geometry of the wind tunnel is considered in the numerical design using ANSYS Fluent code to study the numerical model corresponding to the real geometry. The complete governing equations are available in **Fluent (2006)** [**10**] and a brief overview of these equations is presented here. The general equation of Navier-Stokes equation of the momentum is:

$$\rho\left(\frac{\partial \overline{v}}{\partial t} + \bar{v}.\nabla\bar{v} + \overline{v'.\nabla v'}\right) = B - \nabla\bar{p} + \mu\,\nabla^2\,\bar{v} \quad \ldots\ldots 1.1$$

While the continuity equation can be written as follow:

$$\frac{\partial \bar{p}}{\partial t} = \nabla.(\overline{\rho v} + \overline{\rho' v'}) = 0 \quad \ldots\ldots 2.1$$

The two equations of the turbulent flow $(k-\varepsilon)$ model can be written in two separate equations, one for kinetic energy (k), and the second for the rate of dissipation:

$$\rho\left(\frac{\partial k}{\partial t} + u_j k_j\right) = \left(\frac{\mu_t}{\sigma_k} k_j\right)_j + \mu_t \emptyset - \rho\varepsilon \quad \ldots\ldots 3.1$$

$$\rho\left(\frac{\partial \varepsilon}{\partial t} + u_j \varepsilon_j\right) = \left(\frac{\mu_t}{\sigma_\varepsilon} \varepsilon_j\right)_j + c_1 \frac{\varepsilon}{k}\mu_t \emptyset - \rho c_2 \frac{\varepsilon^2}{k} \quad \ldots\ldots 4.1$$

Where:

$$\emptyset = 2\varepsilon_{ij}\varepsilon_{ij} \quad \ldots\ldots 5.1$$

And:

$$\mu_t = c_\mu \rho \frac{k^2}{\varepsilon} \quad \ldots\ldots 6.1$$

The values of the empirical constantsc_μ, σ_k, σ_ε, c_1 *and* c_2 in the equations (3.1), (4.1) and (6.1) are the default values of 0.09, 1, 1.3, 1.44, and 1.92, respectively.

5.1. Solution Method and Boundary Conditions

The flow quality such as velocity profile, uniformity and turbulent intensity inside the wind tunnel test section has been evaluated based on the boundary conditions shown in **Figure 2**. The outlet boundary condition is designed as an outlets pressure of the wind tunnel itself, while the pressure

Preprints (www.preprints.org) | NOT PEER-REVIEWED | Posted: 19 August 2022 doi:10.20944/preprints202208.0361.v1

losses calculated is designed as fan pressure intake. Then, a comparison was carried out between this model and the experimental results.

The 3-D Reynolds-averaged Navier-Stokes (RANS) and continuity equation are calculated based on CFD commercial code such that control-volume method and the Semi-Implicit Method are used for Pressure-Linked Equations (SIMPLEC) velocity-pressure coupling algorithm with the second order upwind discretisation. A standard k-epsilon model is performed in the numerical simulation [**7, 11, and 12**]. **Figure 2** shows the whole wind tunnel used in CFD as benchmark case (empty test section. Moreover, the numerical simulation boundary conditions are presented in **Table 3**.

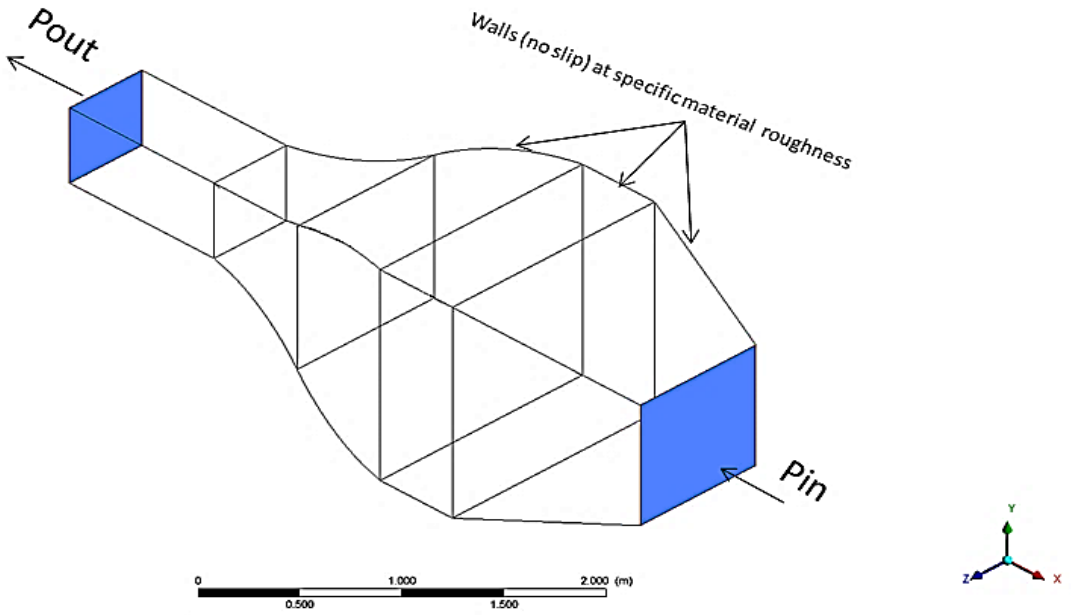

Figure 2: Wind tunnel geometry in CFD.

Table 3: Summery of the numerical simulation boundary conditions.

Parameters	**Set value**
Discretization scheme	Second-order upwind
Algorithm	SIMPLEC
Time	Steady state
Intake fan (pressure loss)	Wind tunnel components losses (Pa)

 doi:10.20944/preprints202208.0361.v1

Pressure outlet	Atmospheric pressure (Pa)
Gravity	-9.81

Furthermore, the modelling of the walls, floor, ceiling and test section took the form of solid walls with asset roughness height and constant. The roughness height associated with the floor, side walls, ceiling, and guide vanes was established as $15x10^{-6}$, while that for the test section was $15x10^{-7}$. The roughness constant was the same for all surfaces – 0.5 **[12, 13].** However, fan blades, the flow straightener section, and mesh screen are not modelled in CFD, while the inlet boundary condition is set as ''fan intake boundary condition''.

5.2. Mesh Structures and Mesh Convergence Study

Both structure and unstructured meshes were used to save computational costs [**12**]. For one-dimensional flow, such as test section, structured prismatic grids were applied. However, for three-dimensional flow with complex structure such as wide-angle diffuser and contraction, tetrahedral/hybrid grids were employed as shown in **Figure 3**. Moreover, **Table 4** provides information about the type of mesh as well as the total number of elements that different wind tunnel sections contained.

Figure 3: Meshing imported to fluent software.

Table 4: Mesh type and distribution in open-jet wind tunnel.

 doi:10.20944/preprints202208.0361.v1

Wind tunnel parts	The type of mesh	Elements number
Wide angle diffuser	Tetra	421875
Settling chamber	Hexa	225000
Contraction	Tetra	450000
Test section (empty)	Hexa	421875
	Total	1518750

Despite being used in different contexts, mesh convergence test and grid independent test have the same context. They are both geared towards the identification of the grid size which is most suitable for a specific problem simulation and allowed grid size to be increased without affecting the solution. A number of different meshes were created with the purpose of analysing mesh independence. The verification of the computational model's programming and the operation was undertaken through grid sensitivity analysis.

In order to assess convergence of the steady-state solution, the monitor check for absolute convergence criteria was turned off for the model, in order to make sure that the solution is converged in the area of interest [16]. The velocity value at two points was monitored throughout the solution until the change in the velocity was less than 0.1 % per iteration.

Two points were created in the domain. The first point is located on the upstream of the test section; which is the interest area where the high velocity may occur, and the second point was in the free stream before the outlet to ensure that no reverse flow occurs during the simulation. These values have been monitored for convergence, while the simulation was running to ensure a steady state solution has been reached. Therefore, it was considered to indicate the convergence of the solution for base line case and for the modified case as well. As we can see after 4750 iteration there is no further changes during the solution, which give us an indication for the convergence for the solution.

Preprints (www.preprints.org) | NOT PEER-REVIEWED | Posted: 19 August 2022 doi:10.20944/preprints202208.0361.v1

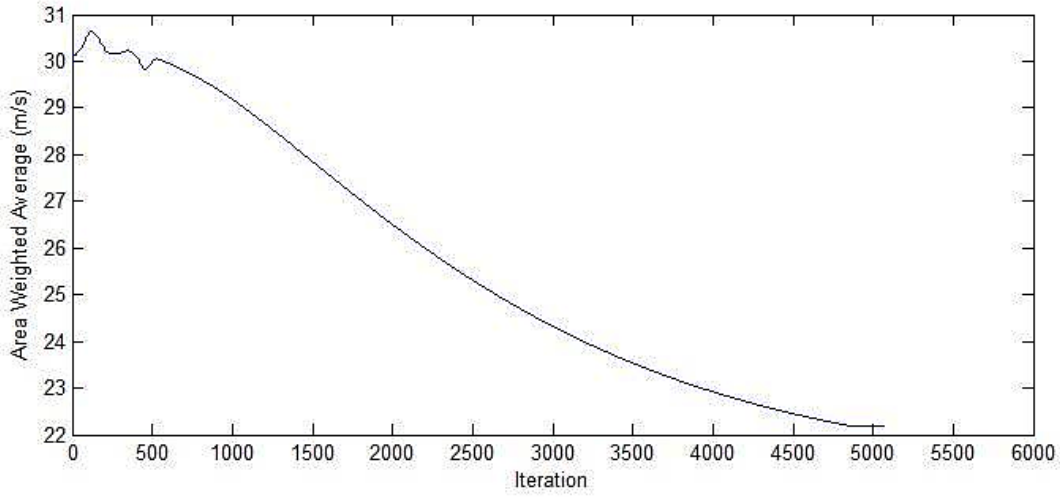

However, despite having "converged" on the basis of RMS error values, monitor points and imbalances, the solution should also be unaffected by mesh resolution, otherwise the CFD results more likely to be inaccurate. It is advised that this procedure be applied at least once for different problem types to enable the use of a similar size of mesh when a similar problem occurs. This increases the result reliability.

In the current study, the wind tunnel was simulated using 1518750 mesh elements while turbulent intensity and average velocity were monitored. **Figure 4** showed these monitored values against the number of cell. It can be seen that the final number of mesh was 1518750 cells based on the mesh dependency study. Turbulent intensity and average velocity were set as monitored values against the number of cell. The convergence of the two parameters with 3-11% imbalances was achieved in the case of 506250 cells. Moreover, a rise in the interest value resulted from the increase in the number of cells to 759375 cells. When the mesh size was increased even more, the simulation of the 1518750 cells produced a value situated in a satisfactory range, of 0.1-0.3%. What this implied was that the mesh resolution had no impact on the value of interest. Therefore, to obtain results within the user-defined range, 1518750 cells were employed in additional analysis.

Preprints (www.preprints.org) | NOT PEER-REVIEWED | Posted: 19 August 2022 doi:10.20944/preprints202208.0361.v1

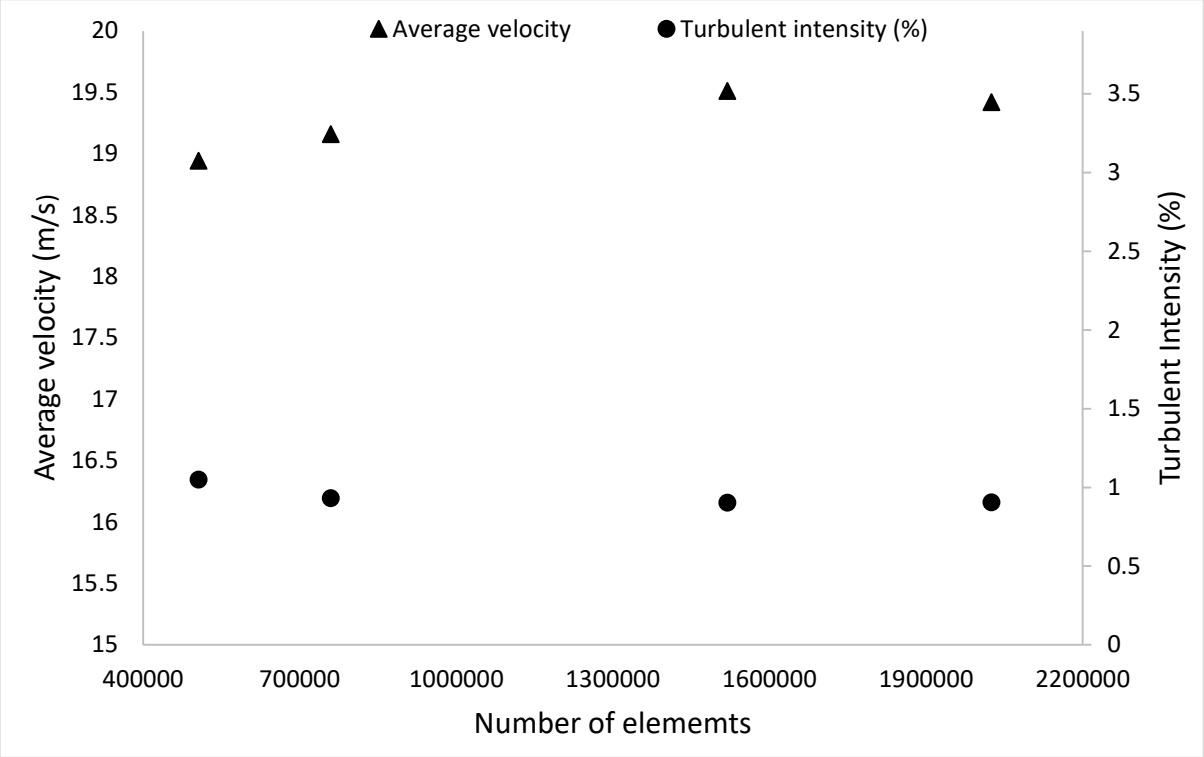

Figure 4: Average velocity and turbulent intensity against number of cells

6. OVERALL LAYOUT OF THE BUILT WIND TUNNEL

The constructed blower wind tunnel is driven by a 5.5 kW centrifugal fan (A Woodchook Ltd fan) which has backward-facing aerofoil type blades. The blower pushes air of 6.25 m^3/s against 650 Pa of static pressure into a wide-angle diffuser via a flexible duct. The diffuser simply is designed consisting of two parts connected though a bolted flange with a maximum angle of 33.4^o with an area ratio of 3:1. Two permeable screens of 0.67 porosity are set between both diffusers while another screen is set at the exit of the second diffuser. A settling chamber is used to merge the airflow of the two branches before it passes through the contraction segment of the wind tunnel. The honeycomb with a thickness of 100 mm is placed at the inlet of the settling chamber followed by three mesh screens with a sufficient space of 100 mm. This should also be the dimension of the space between the last screen and the contraction. The contraction section has a contraction ratio (CR) of 7.8:1 over a length of 160 cm. The final-constructed wind tunnel is shown in **Figure 5**.

 doi:10.20944/preprints202208.0361.v1

Figure 5: The final constructed layout of the built open-jet wind tunnel.

7. EXPEREMTNAL METHODOLOGY

Two different wind tunnel configurations were introduced in this research as shown in **Figures 6a, and b**. The first configuration was the benchmark configuration in which no convex hump model was presented (empty test section). The test section middle slot was covered with an appropriate designed Perspex plate to ensure no leak could occur during the operation as shown in **Figure 6a**. This configuration was utilised to evaluate the flow quality on the test section in terms of turbulent intensity, velocity profile and flow uniformity comparing to CFD results.

The second configuration involved the attachment of a convex hump model of length, width and height 500 × 200 × 30 mm^3 respectively, located centrally to the wind tunnel test section through a rectangular slot in the wind tunnel bottom plate as shown in **Figure 6b**. This rectangular slot had a 60^o cutting angle to avoid any contact between the hump edge and the test section that may damage the Perspex material. This second test is allowed to examine the suitability of the constructed wind tunnel in aerodynamic research and/or achieving the flow characteristics for which blower tunnel is designed using both hot-wire anemometer (HWA).

Preprints (www.preprints.org) | NOT PEER-REVIEWED | Posted: 19 August 2022 doi:10.20944/preprints202208.0361.v1

Figure 6: a- benchmark wind tunnel configurations (solid works and real setup) b-convex hump attached to the wind tunnel test section (solid works and real setup).

7.1. Empty Test Section Setup and Measurement Techniques

The purpose of the initial experiment was conducted with an empty test section to measure the velocity inside the test section using a pitot static tube and calibration the wind tunnel test section velocity against motor frequency. Then the wind tunnel performance was evaluated using a single hot wire anemometer to determine the uniformity of velocity distribution at the test section, and whether it displayed the appropriate turbulence intensity.

The hot-wire anemometer measurements were conducted by the means of IFA 300 with single probe (Dentec Dynamic type 55M11) fixed in the stainless-steel probe support of 4 mm outer diameter (see **Figures 7a and b**). The probe was introduced into the flow by the manual three-axis traverse fixed on test section. This traverse was mounted on a key clamp frame on the test section outlet flange as indicated in **Figure 7c** such that the whole traverse could be moved horizontally, vertically and Z

Preprints (www.preprints.org) | NOT PEER-REVIEWED | Posted: 19 August 2022 doi:10.20944/preprints202208.0361.v1

coordinates over a stream-wise distance of approximately 1, 0.5, 0.5 m respectively. Therefore, fine movements of less than 3 mm in the x, y and z directions could be accomplished by using this manual traverse.

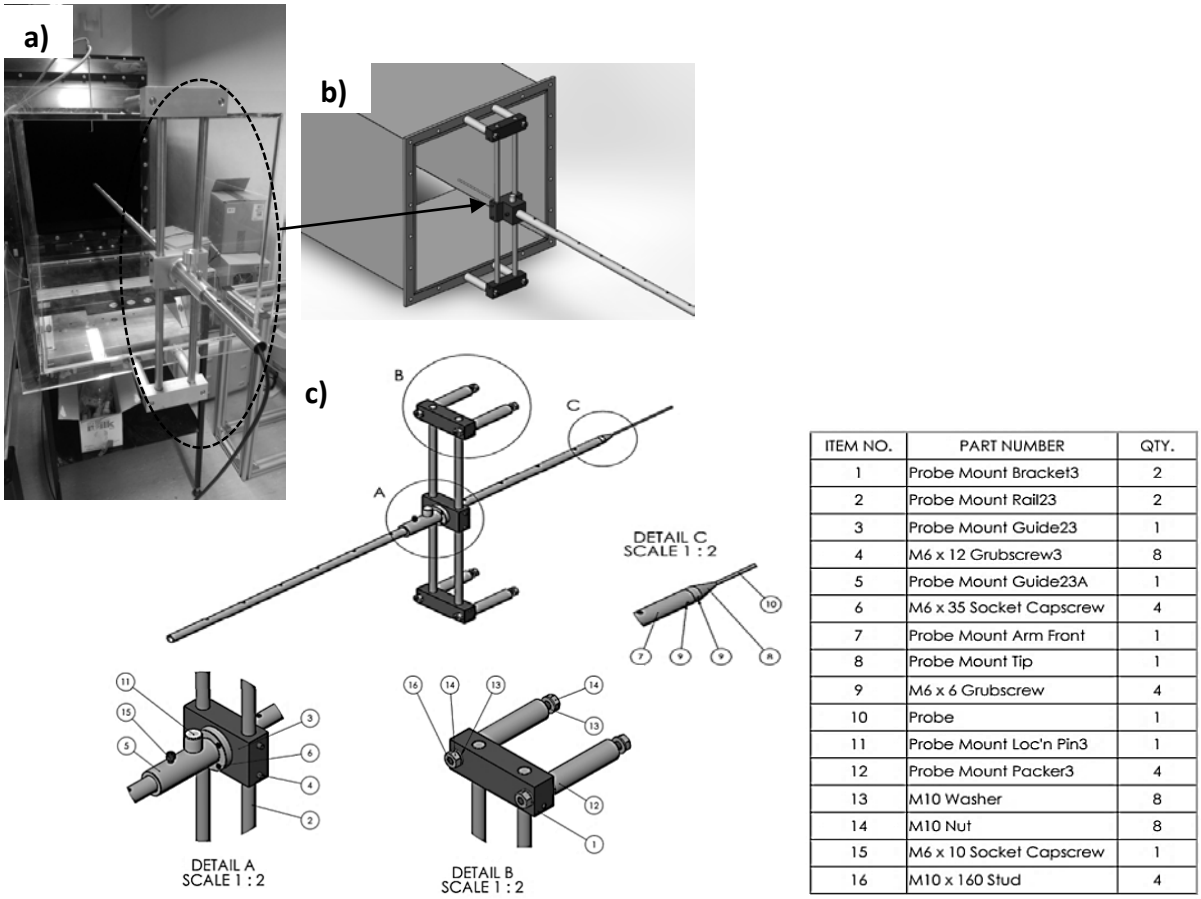

ITEM NO.	PART NUMBER	QTY.
1	Probe Mount Bracket3	2
2	Probe Mount Rail23	2
3	Probe Mount Guide23	1
4	M6 x 12 Grubscrew3	8
5	Probe Mount Guide23A	1
6	M6 x 35 Socket Capscrew	4
7	Probe Mount Arm Front	1
8	Probe Mount Tip	1
9	M6 x 6 Grubscrew	4
10	Probe	1
11	Probe Mount Loc'n Pin3	1
12	Probe Mount Packer3	4
13	M10 Washer	8
14	M10 Nut	8
15	M6 x 10 Socket Capscrew	1
16	M10 x 160 Stud	4

Figure 7: a- Wind tunnel with empty test section, b- Hot wire anemometer probe traversing design c- Hot wire probe support parts design.

The hot-wire anemometer was also used to measure the air velocities fluctuating and turbulence intensity inside an empty test-section. Wind speed measurements were achieved along 15 perpendicular lines located on five planes in the test section (L1–L15), at intervals of 0.25 m (horizontal) and 0.83 m (perpendicular) with one horizontal plane as shown in **Figure 8** and **Table 5**. These points then were then compared with the CFD results. The experimental and numerical results of the data were presented in results and discussion section.

Preprints (www.preprints.org) | NOT PEER-REVIEWED | Posted: 19 August 2022 doi:10.20944/preprints202208.0361.v1

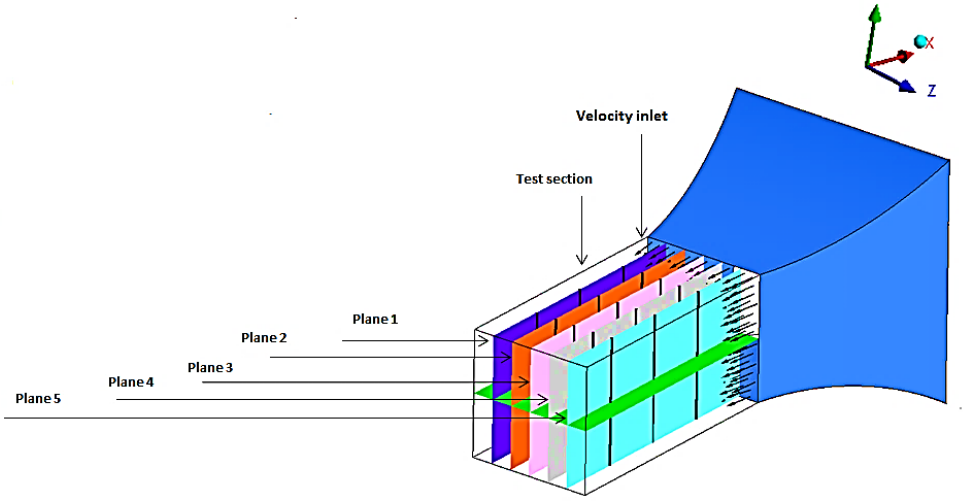

Figure 8: Measurement lines coordinates and planes.

Table 5: Summary of the measurement point co-ordinates

Plane/Lines	X (mm)	Y (mm)	Z (mm)
Plane 1 / L1	0	0 - ± 250	166
L2	250	0 - ± 250	166
L3	-250	0 - ± 250	166
Plane 2 / L1	0	0 - ± 250	83
L2	250	0 - ± 250	83
L3	-250	0 - ± 250	83
Plane 3 / L1	0	0 - ± 250	0
L2	0	0 - ± 250	0
L3	0	0 - ± 250	0
Plane 4 / L1	0	0 - ± 250	- 83
L2	250	0 - ± 250	- 83
L3	-250	0 - ± 250	- 83
Plane 5 / L1	0	0 - ± 250	- 166
L2	250	0 - ± 250	- 166
L3	-250	0 - ± 250	- 166

Preprints (www.preprints.org) | NOT PEER-REVIEWED | Posted: 19 August 2022 doi:10.20944/preprints202208.0361.v1

7.2. Wind Tunnel Test Section with Convex Hump Model

Two sets of experiments were carried out when the convex hump model is inserted. The first, a HWA was used to evaluate the power spectral density (PSD) and fluctuated velocity behind a convex hump model to provide quantitative measurements of the vortex shedding which is a method of representing the frequency content of velocity signals into the hump wake region. This velocity signal was measured in the wake area downstream of the hump model at locations varied from $X/L = 1$ and $Y/h = 0$ *to* $Y/h = 3$ respectively (see **Figure 9)**, at different free stream velocity varying from U_∞ = 6 m/s to U_∞ = 10 m/s. After the signal was captured, a Fast Fourier transform (FFT) was performed to convert the data from time domain into spectral data using the MATLAB program in order to obtain the power spectral in the wake region.

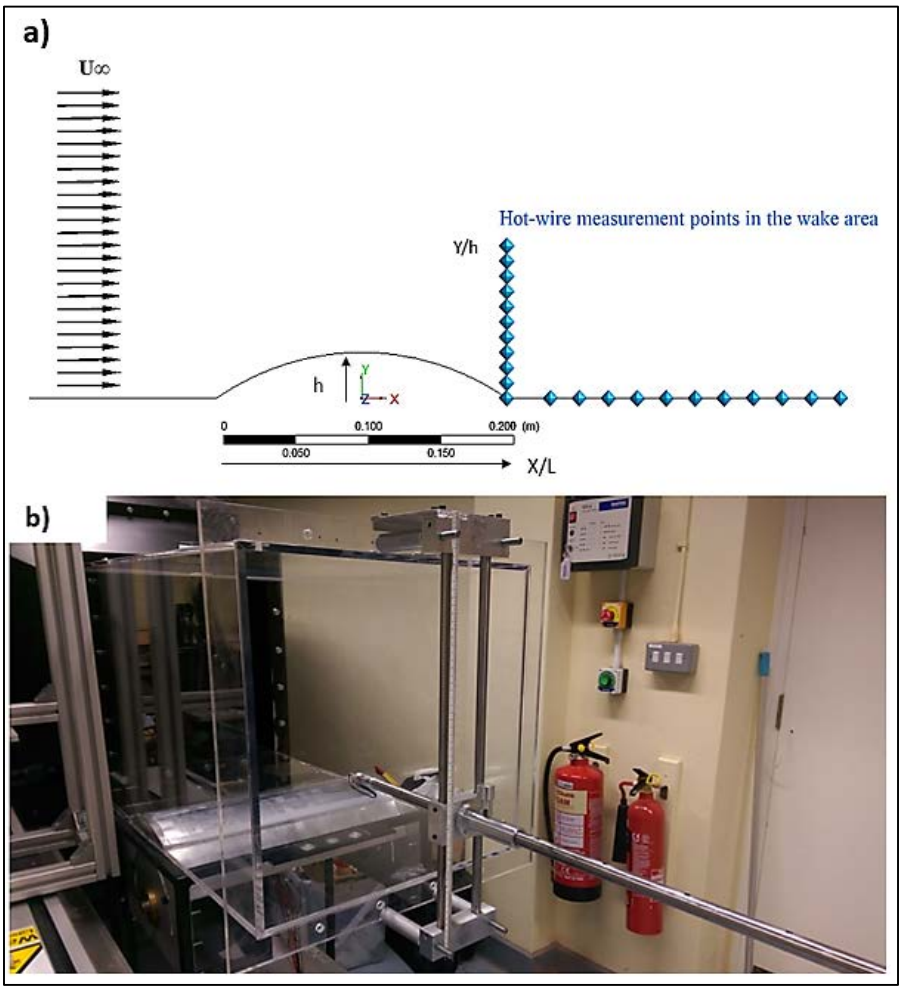

Figure 9: a) co-ordinate system in the measurement area; b) Experimental set-up in the wind tunnel.

Preprints (www.preprints.org) | NOT PEER-REVIEWED | Posted: 19 August 2022 doi:10.20944/preprints202208.0361.v1

8. RESULTS AND DISCUSSION

8.1. Empty Test Section Assessments

The test section velocity is controlled by varying the fan rotation frequency (rpm). The wind tunnel is designed to operate in an adjustable and stationary speed range from 2 m/s to about 20 m/s with motor frequency range from 5 Hz up to 45 Hz. The variable frequency driver (VFD) responds to control signals from the remote keypad. The velocity has a linear fitted line against frequency as shown in **Figure 10**, which clearly showed that the motor frequency increased linearly with the velocity of the wind tunnel. This test will help in any aerodynamic test in future such that any velocity can be selected with the corresponding motor frequency.

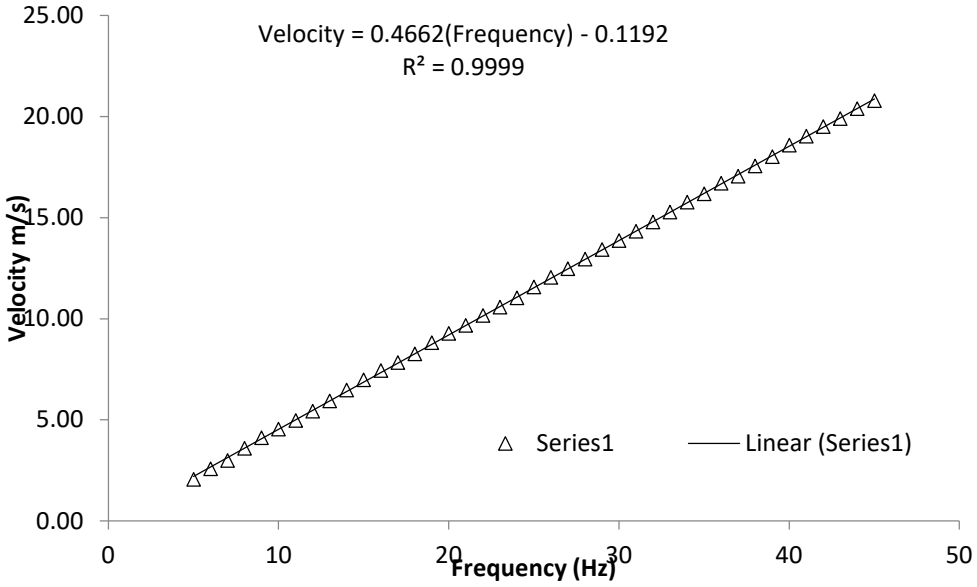

Figure 10: Wind tunnel velocity (m/s) against frequency (Hz).

Prior to the wind tunnel performance measurements, a study of determining the acceptable sampling parameters such as sampling frequencies, sampling periods and software check for the hot wire anemometer used here was conducted using circular cylinder model. The test on the circular cylinder is shown in **Figures 11a and b**. The cylinder has 25 mm in diameter. One end of the cylinder can be linearly adjusted which helps to place it horizontally in the middle between the wind tunnel side walls.

The hot-wire probe was mounted behind the circular cylinder in the wake flow at a distance of one diameter. It was traversed in x, y direction to measure the velocity fluctuation signal level (RMS) at

Preprints (www.preprints.org) | NOT PEER-REVIEWED | Posted: 19 August 2022 doi:10.20944/preprints202208.0361.v1

different sampling frequencies and sampling period. The wind tunnel speed was set of 12 m/s, which gave Reynolds number of Re = UD/v = 1.6 x 10^4 (~ critical flow). This test is to examine whether the cylinder is shedding the vortices with a 'right' frequency based on the circular cylinder diameter or not, and the non-dimensional Strouhal number ($St = f \times D / U_\infty$) which should be in the order of about 0.19.

The comparison of power spectral density (PSD) with and without the wake flow behind the cylinder was summarized in **Figure 12**. The frequency spike on the power spectrum plot was indicated the existence of vortex shedding in the wake flow due to the flow separation. The Strouhal number estimated from the figure was 0.189 (f ≈ 91 Hz) for the range of sampling frequency varied from 1000 to 10000 Hz. Therefore; it can be concluding that the wind tunnel performance can be tested at sampling frequencies from 1000 up to 10000 Hz with an optimal processing resolution at 8192 points for determining the frequency spike.

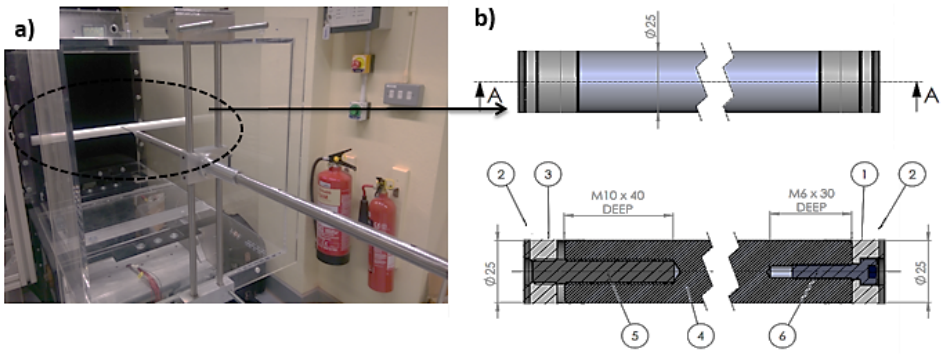

ITEM NO.	PART NUMBER	QTY.
1	Fixed Pad	1
2	Nitrile Pad	2
3	Adjustable Pad	1
4	Test Section Insert	1
5	M10 x 52 Stud	1
6	M6 x 25 Socket Capscrew	1

Figure 11: a- Hot-wire with circular cylinder installed, b- Schematic view of circular cylinder design.

Preprints (www.preprints.org) | NOT PEER-REVIEWED | Posted: 19 August 2022 doi:10.20944/preprints202208.0361.v1

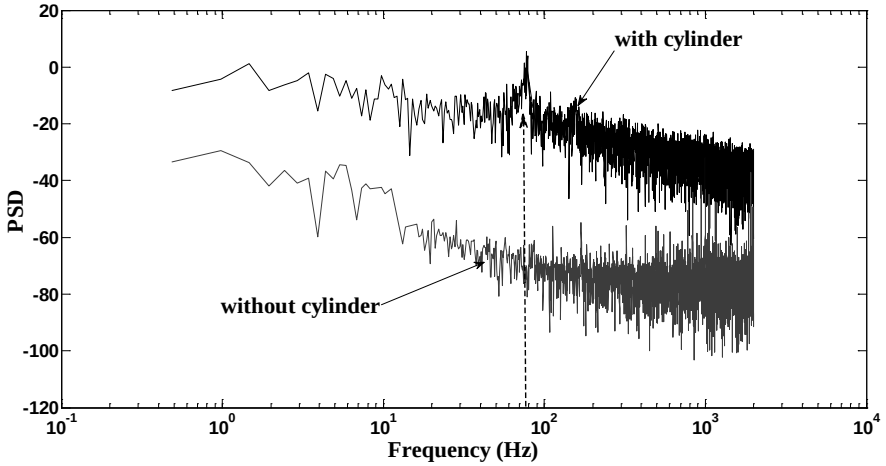

Figure 12: Power spectral density with and without circular cylinder at sampling frequency = 4000 Hz.

The turbulent intensity of the constructed wind tunnel in 5 planes and 15 lines in total as a function to the height of the test section can be distinctly seen in **Figures 13 planes 1 to 5**. By comparison to the CFD results, the turbulent intensity was considerably reduced from 1.8% to 0.6% at freestream velocity of 19 m/s. This reduction in the turbulent intensity is caused by the introduction of boundary layer controls. These control devices such as honeycomb and mesh screens had been equipped inside the wide-angle diffuser and settling chamber of the constructed wind tunnel, but the CFD model had not, which could explain the findings obtained. Therefore, flow separation on the wind tunnel corners, which exerts a significant effect on the flow quality within the test section, was responsible for the turbulent intensity increase observed in the CFD data. Therefore, the experimental results showed the benefit of using boundary layer controls inside the constructed wind tunnel in reducing the turbulent intensity by up to 50% compared to CFD results.

Preprints (www.preprints.org) | NOT PEER-REVIEWED | Posted: 19 August 2022 doi:10.20944/preprints202208.0361.v1

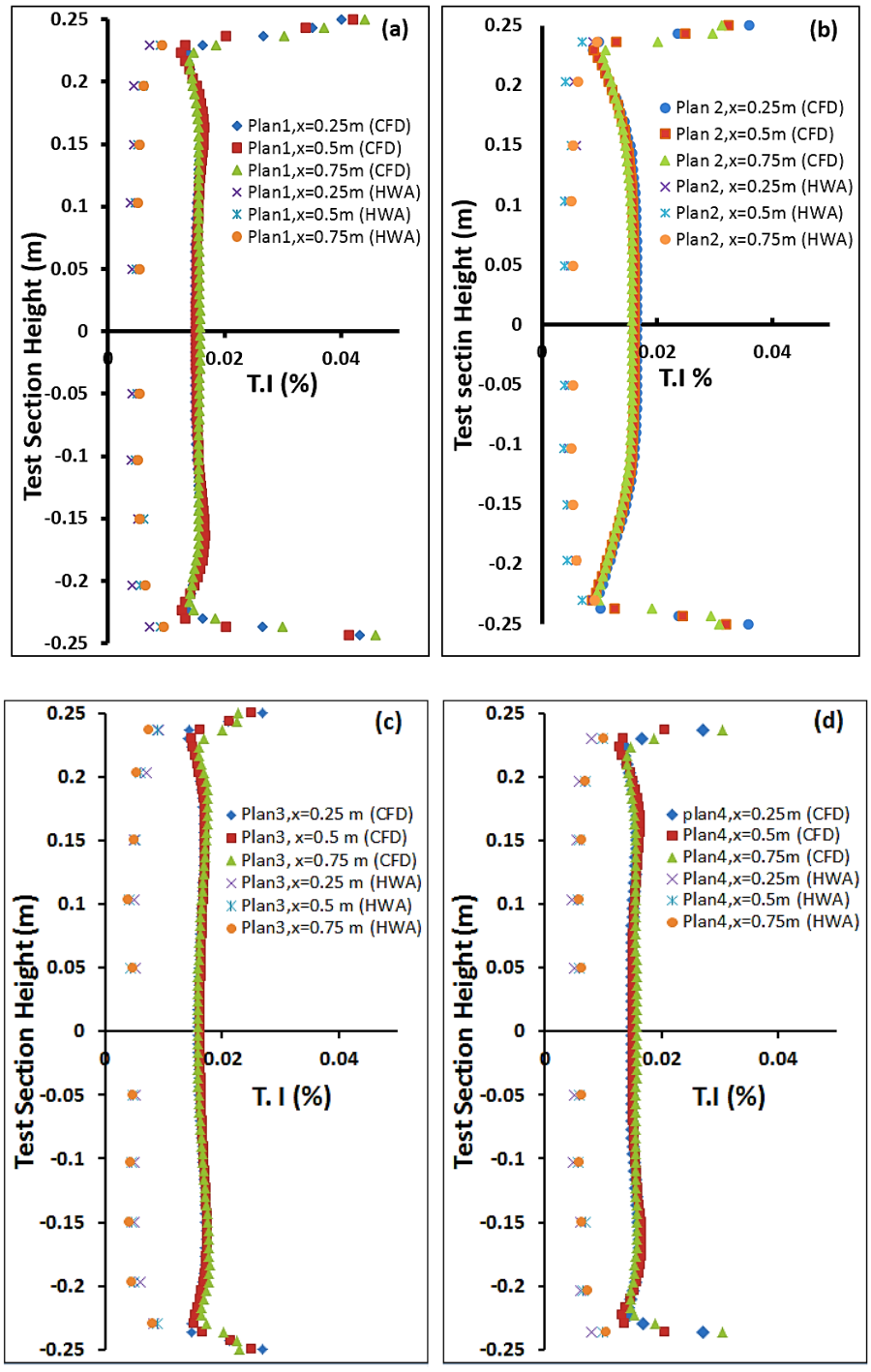

Preprints (www.preprints.org) | NOT PEER-REVIEWED | Posted: 19 August 2022 doi:10.20944/preprints202208.0361.v1

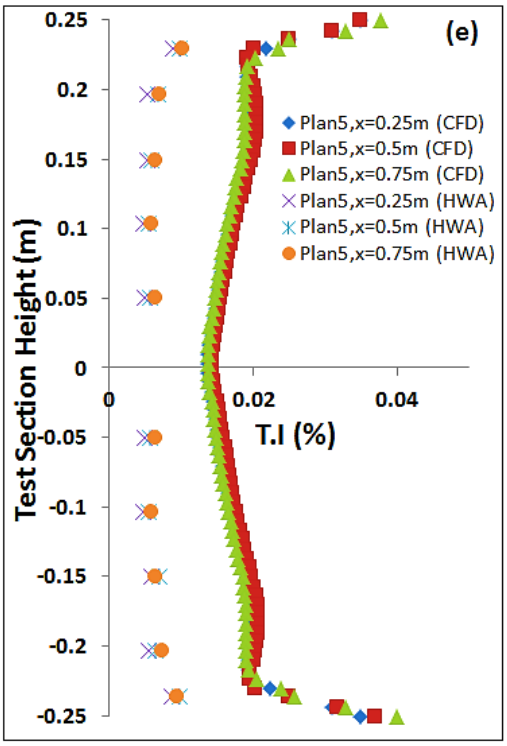

Figure 13: Experimental and numerical turbulent intensity results of the flow at the positions planes 1-5 for the free stream velocity of 19 m/s.

Figure 14 shows an experimental and CFD results comparison of the centreline turbulence intensity with stream-wise distance in the wind tunnel at velocity of 19 m/s. Similarly, the figure was illustrated the positive effect that the conditioning devices had on flow turbulent intensity levels and velocity variation. The figure clearly showed that throughout the test section of the constructed wind tunnel, the turbulence intensity was diminished by nearly 0.9 orders of magnitude compared to CFD case, which approached the desired value. The most likely reason for this is due to the conditioning devices (honeycomb, mesh screen and settling chamber) that were carefully designed and inserted inside the wind tunnel, which not been considered in CFD model such that the flow separation on the wind tunnel corners have large impact on the flow quality inside the test section.

The mesh screens were placed in five different points which may break up large turbulent eddies into small-scale hence reduced the turbulent intensity levels of the incoming flow. Moreover, the honeycomb has more likely to remove the swirl and minimise the lateral turbulence in the flow by forcing small sections of the flow to straighten through small hex-tube cells hence increasing the flow uniformity inside the test section. The honeycomb used here had a significant impact on the

Preprints (www.preprints.org) | NOT PEER-REVIEWED | Posted: 19 August 2022 doi:10.20944/preprints202208.0361.v1

flow due to its length of 6-8 times the size of the cell and positioning at 100 mm upstream of the next three screens which been strongly recommended by **Smith [14]**.

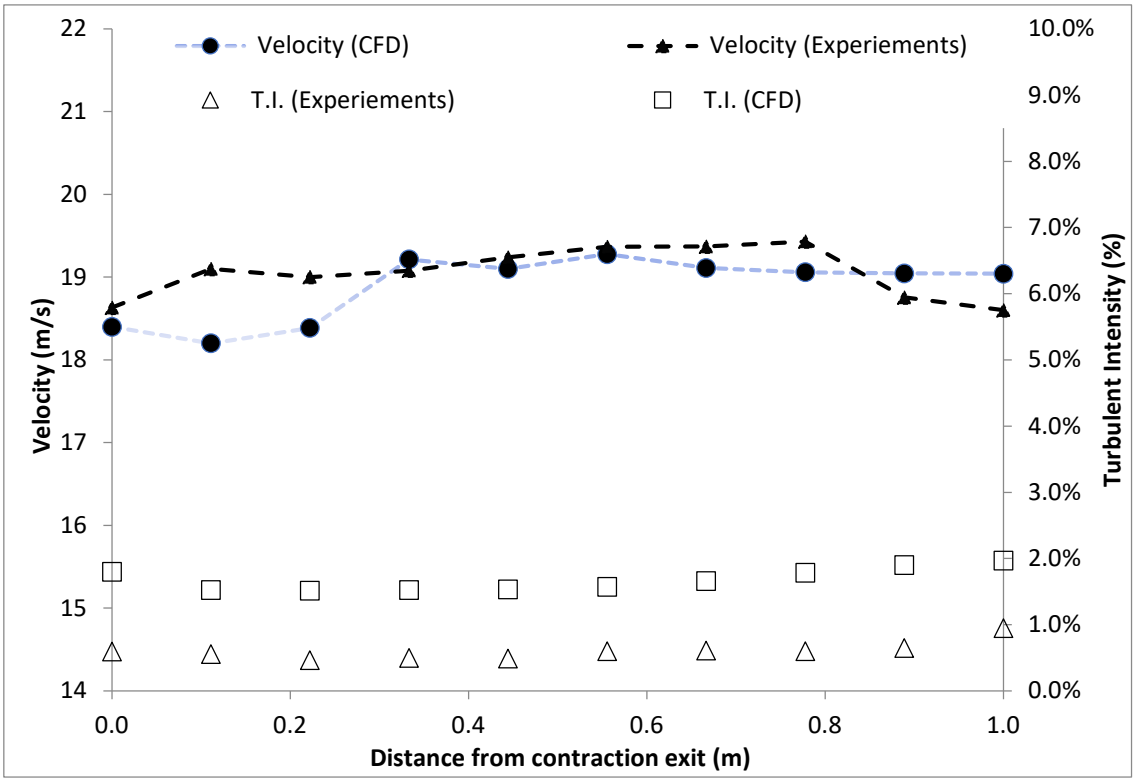

Figure 14: Comparison of centreline velocity and turbulence intensity of CFD and experimental results.

Figure 15 shows the stream-wise air velocity contour of the whole the wind tunnel parts, with the convex hump model and boundary layer controls being not considered. The flow separation on the wind tunnel corners caused the velocity variation at test section start and end for CFD case to exceed that in the experimental case and increased from 1.7% to 4.2% respectively at 19 m/s velocity. Flow separation at the corners was markedly increase the velocity variation inside the test section, however, when the boundary layer controls were inserted, the flow quality was significantly increased by about 33.5% compared to CFD model.

Consequently, over the entire length of the test section, the flow exhibited good flow quality mainly in terms of turbulent intensity, while the airflow distribution within the wind tunnel circuit was also satisfactory, in keeping with the expectations set for the designed wind tunnel. Moreover, the test section velocity was not as homogenous as expected in CFD, the top and bottom area of the tunnel diffuser revealing a higher fluctuated velocity as shown in the figure below. Therefore, more

 doi:10.20944/preprints202208.0361.v1

future work is needed to validate the flow quality when the mesh screen and honeycomb will be added to the CFD model as a porous media.

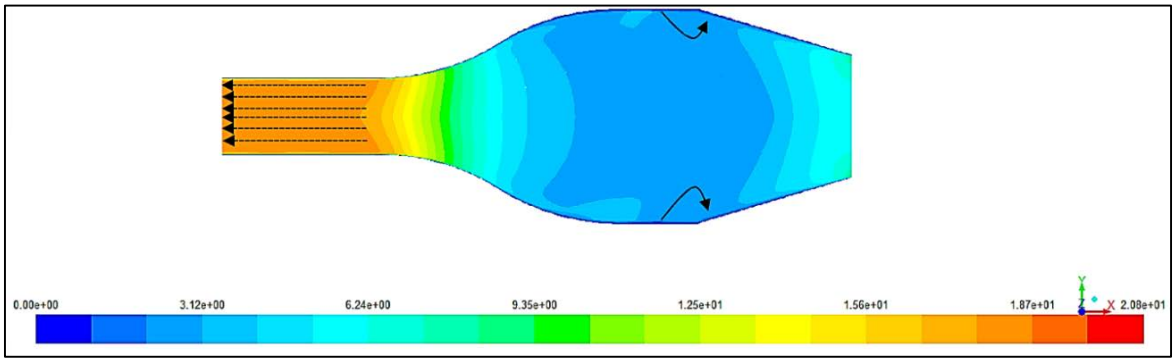

Figure 15: Contour of velocity magnitude.

Figure 16a and b compare a normalised of velocity profile at locations of 0.25 m and 0.75m at two various velocities 19 m/s and 4 m/s in stream wise (x) direction. As a result, it can be surmised that the flow quality was essentially uniform within the major part of the test section region along the test section height with maximum deviation of velocity of 2.5%. An improvement in flow quality was achieved by adding the flow conditioning devices. Throughout the test section, the turbulence intensity was diminished to 0.6%, which approached the desired value. Therefore, to validate the suitability of the current wind tunnel for an aerodynamic research, additional experimental tests over the hump model were carried out.

Preprints (www.preprints.org) | NOT PEER-REVIEWED | Posted: 19 August 2022 doi:10.20944/preprints202208.0361.v1

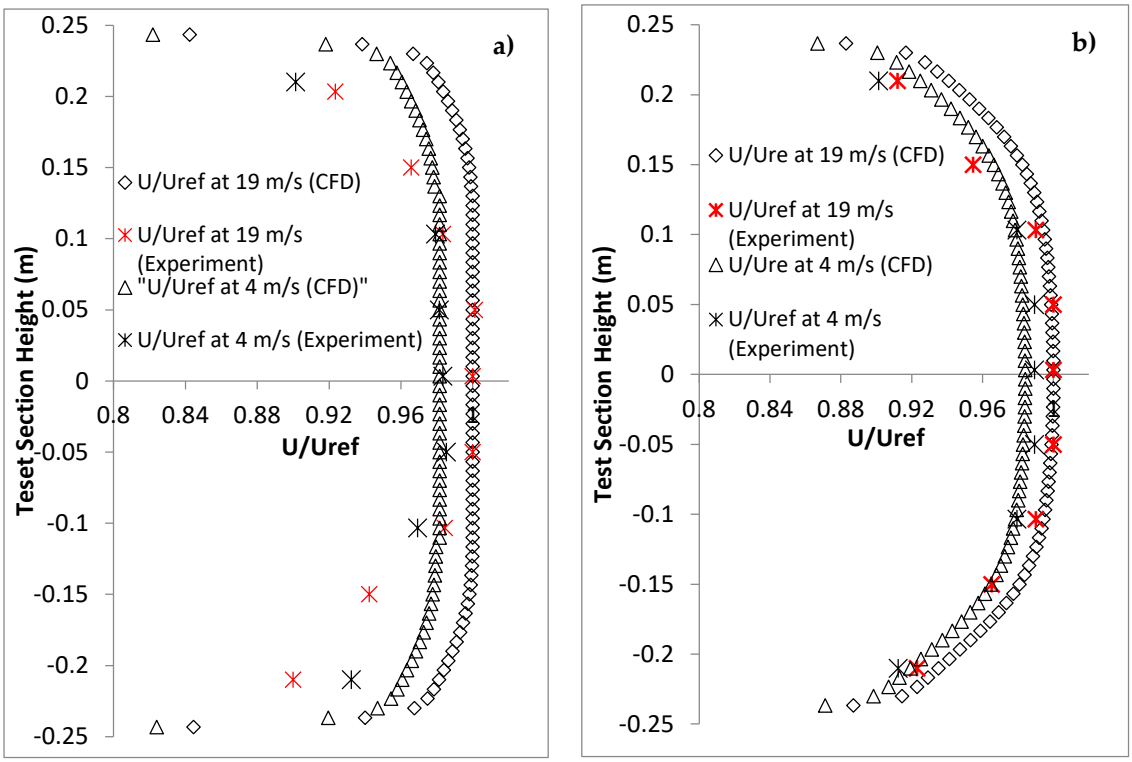

Figure 16: Comparison between CFD and experimental data of the dimensionless velocity profile in plan 3 at (a- X = 0.25 and b- X = 0.75m).

8.2. Wake Flow Investigation Behind the Hump Model

Firstly, the PSD results of the time-averaged velocity signals versus Y/h and X/L downstream of the convex hump are also shown in **Figures 17a and b** at free-stream velocity of 7 m/s. These figures introduce a comparison of both mean velocity and PSD at $X/L = 1$ and $Y/h = 0$ (inside the wake area) and the mid-test section. The figures have shown the major contribution to the unsteady lateral motion flow which creates a high fluctuation in velocity over the mean velocity at any given point close to the hump inside the wake region due to the separation incipient over the convex hump surface. This velocity fluctuation inside the wake area ranged between zero and positive values due to the hot-wire probe not being sensitive to the flow direction and thus reversing any negative signals.

However, considerable differences can be observed in **Figure 17b**. The highest energy of the flow has been found for $Y/h = 0$ which indicates that the flow became highly unsteady as a result of the flow separation incipient. This energy of the flow became lower as the hot-wire probe moved

Preprints (www.preprints.org) | NOT PEER-REVIEWED | Posted: 19 August 2022 doi:10.20944/preprints202208.0361.v1

towards the wind tunnel mid-test section until the turbulence became less than 1, suggesting that the probe was out-side of the wake area behind the convex hump.

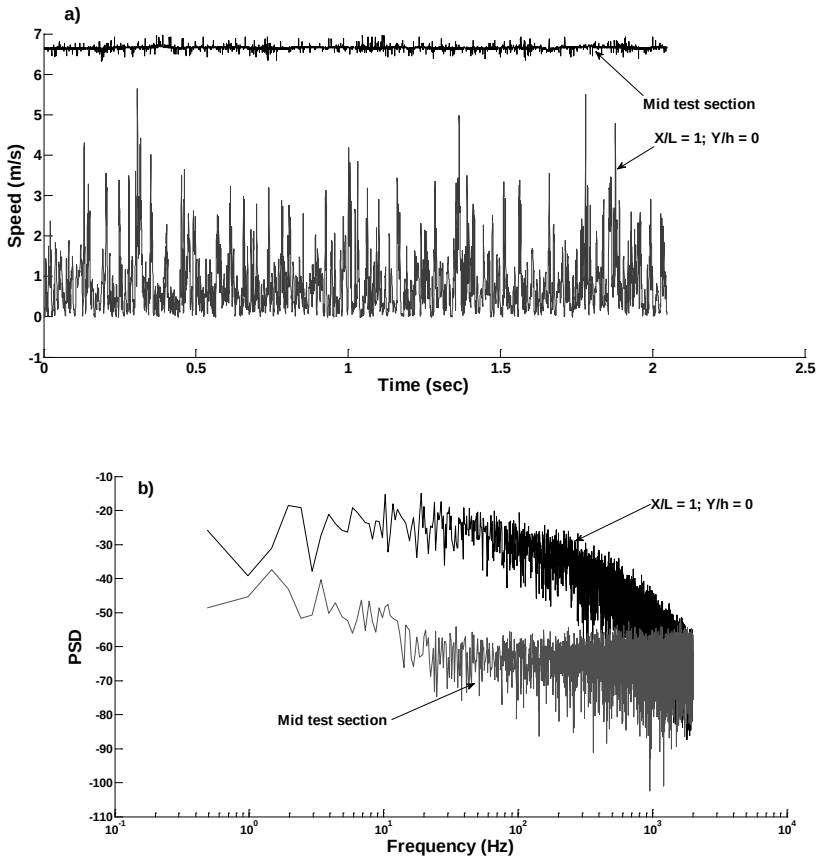

Figure 17: a) Velocity deficit and b) PSD in the wake area and mid-tunnel section.

Figures 18a to d show that the PSD distributions of the fluctuated velocity signal for the hot-wire probe moved from $Y/h = 0$ to 3 having the same location of $X/L = 1$ in the wake region of the convex hump at the four freestream velocities. At $Y/h = 0.5$, the energy of the flow became lower and the spikes of the spectral peaks were clearly seen in this region suggesting that the probe was inside the vortex shedding area behind the convex hump. However, a dominant spectral peak is located at $Y/h = 0.5$ in the wake region that exists about $f_s = 66.4$ Hz at 6 m/s freestream velocity, which is more likely to indicate that a vortex shedding (f_s) is generated downstream of the convex hump. Similarly, the experiments were repeated at the same locations for three different freestream velocities of U_∞ = 7, 8 and 10 m/s, which is illustrated in **Figures 16b to d**. Again, the figures clearly show that at the given Y/h location, the expected spikes of the vortex shedding are clearly seen.

Preprints (www.preprints.org) | NOT PEER-REVIEWED | Posted: 19 August 2022 doi:10.20944/preprints202208.0361.v1

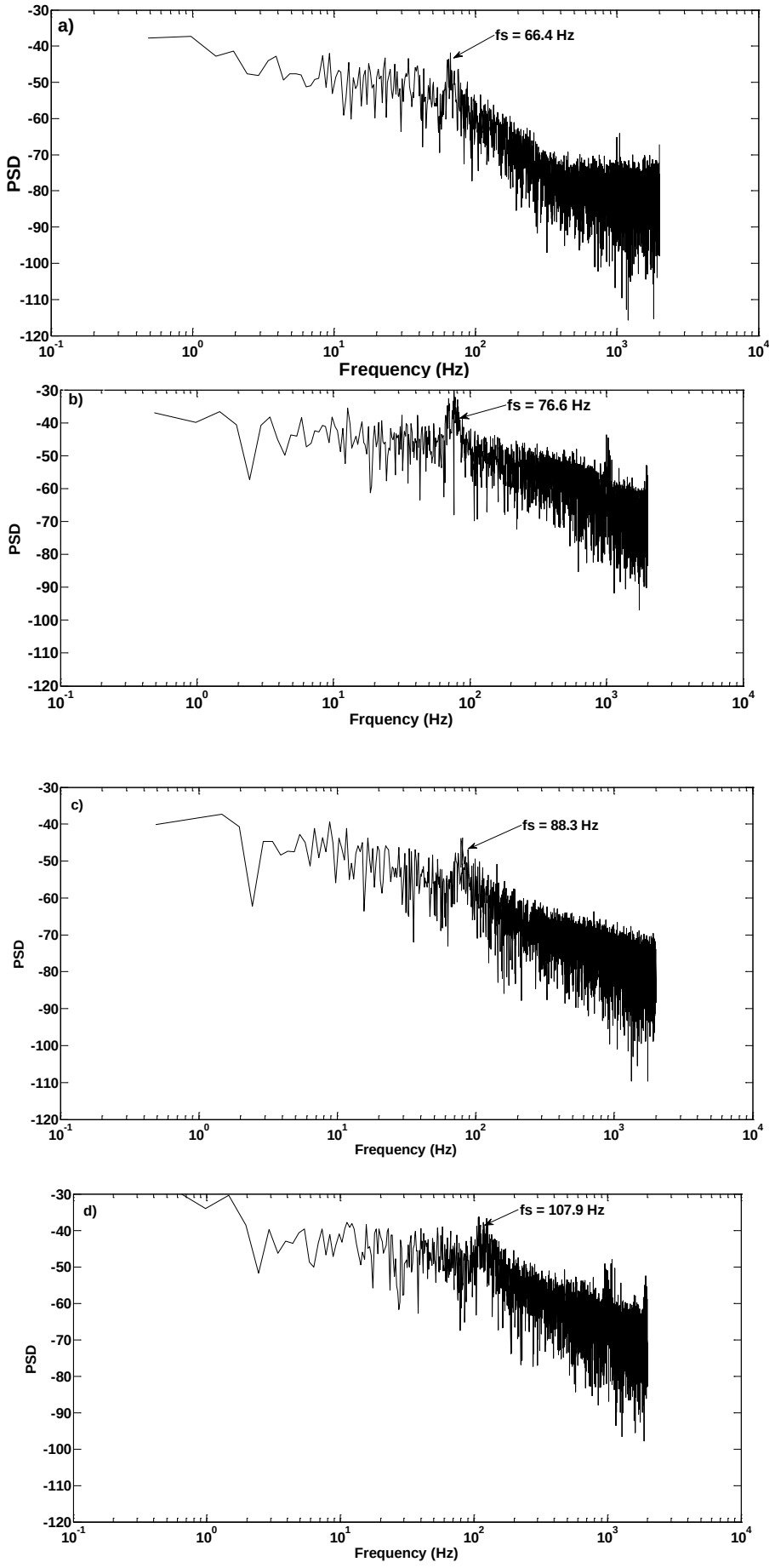

Figure 18: Power spectral density at a) U_∞ = 6 m/s; b) U_∞ = 7 m/s; c) U_∞ = 8 m/s; (Y/h = 0.5); d) U_∞ = 10 m/s; (Y/h = 0.5).

As shown in the previous figures, with the increasing of the freestream velocities from 6 to 10 m/s, the vortex shedding frequency also increased. This increase agreed with results obtained by other researchers [15, 16]. Therefore, a linear relationship between the freestream velocity and vortex shedding frequency can be seen in **Figure 19**. The figure clearly shows that the dominant peaks of f_s = 76.6, 88.3 and 107.9 respectively occurred about the same value of Y/h = 0.5.

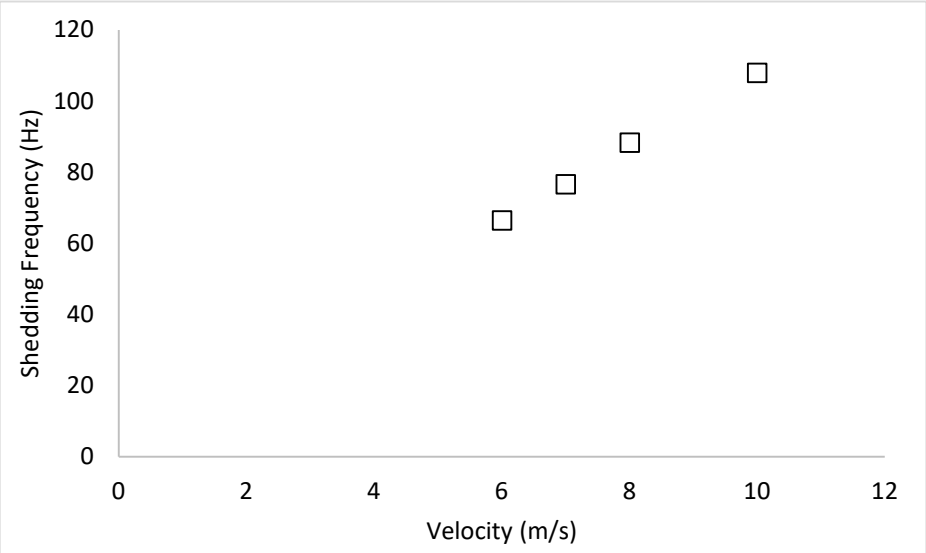

Figure 19: Vortex shedding frequency vs freestream velocity.

Additionally, the oscillating flow can be described by a common non-dimensional number to identify the characteristic associated with the vortex shedding frequencies which is named the Strouhal number which is defined as:

$$St = \frac{f_s \times D}{U_\infty} \dots\dots\dots\dots\dots\dots\dots\dots\dots\dots\dots\dots\dots\dots\dots\dots\dots\dots\dots\dots\dots\dots\dots\dots\dots\dots\dots..7.1$$

where f_s is the vortex shedding frequency of the given freestream velocity, D is the diameter (represented by height in the present hump) and U_∞ is the freestream velocity. The convex hump height is 30 mm and the vortex shedding frequencies based on the four freestream velocities are 66.4, 76.6, 88.3 and 107.9 Hz resulting in a Strouhal number of about 0.31.

 doi:10.20944/preprints202208.0361.v1

9. CONCLUSION AND FUTURE WORK

A new low-speed open-circuit wind tunnel has been designed and constructed at the University of Leeds with test section dimensions of 1m × 0.5 m × 0.5 m (Length × Width × Height). A series of Computational Fluid Dynamic (CFD) models and experimental evaluations were conducted to determine the flow quality and to verify the wind tunnel adequacy for aerodynamic studies [17]. Analysis of the flow quality results in an empty test section showed that adding flow conditioning devices (five mesh screens and one honeycomb) to the constructed wind tunnel reduced the turbulent intensity by more than 50 % compared to both CFD case results at 19 m/s. An improvement in flow quality is achieved by adding flow conditioning devices. Throughout the test section, the turbulence intensity is diminished to approximately 0.6% compared to CFD results, which approached the desired value.

This represents a significant endorsement of flow conditioning devices, illustrating that design focus should concentrate on the settling chamber boundary layer controller – especially where it aligns with the test section. Some useful guidelines can be derived from this chapter for the requirement of wind tunnel design. Therefore, to validate the suitability of the current wind tunnel for aerodynamic research, additional experimental tests behind convex hump were carried out.

The velocity fluctuation profile and PSD behind the convex hump were evaluated using hot wire anemometer and PIV at different freestream velocity. The results clearly showed that the PSD results are generally broadband in nature except for dominant spectral peaks centred at a Strouhal number of 0.31 which is associated with the separated flow region. From here, it can be concluded that the blower wind tunnel is ready for engineering research.

APPENDEX –A

Table A1: Airflow quality examined and measurement devices.

Measurement Relation	**Method**	**Tools**	**Relevant**

 doi:10.20944/preprints202208.0361.v1

Velocity (m/s)	Empty test section at ten points	Pitot static tube and hot-wire anemometer, (IFA-300), [7]	$U_\infty = \sqrt{\frac{2 \times \Delta P}{\rho}}$
Turbulent Intensity (%)	Empty test section	Hot-wire anemometer, (IF-300), [18]	$T.I = \frac{\sigma_v}{\overline{u}}$
Flow Symmetry	The velocity profile was measured with tunnel heights	Hot-wire anemometer, (IFA-300), [12]	$Symmetry = \frac{U_i}{u_{max}}$
Velocity Deviation	The velocity variation with test section height	Hot-wire anemometer, (IFA-300).	V.D = ΔU/U∞

REFERENCES

[1] Azzawi, Itimad DJ, X. Mao, and Artur J. Jaworski. "Design, fabrication and characterization of low speed open-jet wind tunnel." In Proceeings of World Congress on Engineering 2016, vol. 2, pp. 883-888. Newswood Limited, 2016.

[2] Mehta, R., Bradshaw P., "Design rules for small low-speed wind tunnels." *Aeronautical Journal* 83.827 (1979): 443-449.

[3] Itimad D. J. Azzawi; Ahmed F. Hasan., "Comparison and optimization design methodology for open-loop subsonic wind tunnel". 1st International Scientific Conference of Engineering Sciences - 3rd Scientific Conference of Engineering Science (ISCES), 2018, Pages: 186 - 191

[4] Clauser, F., "Turbulent boundary layers in adverse pressure gradients." *Journal of the Aeronautical Sciences* (2012).

[5] Westphal, R., Eaton J.,Pauley W., "Interaction between a vortex and a turbulent boundary layer in a streamwise pressure gradient."*Turbulent Shear Flows 5*. Springer Berlin Heidelberg, 1987. 266-277.

[6] Schwarz, W., and Peter B., "Measurements in a pressure-driven three-dimensional turbulent boundary layer during development and decay." *AIAA journal* 31, no. 7 (1993): 1207-1214.

[7] Calautit, J. K., Hassam N., Ch., Ben R. H., Lik F. S., "A validated design methodology for a closed-loop subsonic wind tunnel." *Journal of Wind Engineering and Industrial Aerodynamics* 125 (2014): 180-194.

[8] Nader, G., Dos Santos, C., Jabardo, P., Cardoso, M., Taira, N., Pereira, M., 2006. Characterization of low turbulence wind tunnel, Metrol. Sustain. Dev. Rio de Janeiro, Brazil, pp. 17–22. (September).

[9] Mehta RD. The aerodynamic design of blower tunnels with wide-angle diffusers. Progress in Aerospace Sciences. 1977 Jan 1; 18:59-120.

[10] FLUENT Incorporated: FLUENT user guide [online] 2006. Available from: www1. ansys.com (accessed 01.02.12).

[11] Gartmann, A., Wolfgang F., Wolfgang S., and Mathias D., "CFD modelling and validation of measured wind field data in a portable wind tunnel." *Aeolian Research* 3, no. 3 (2011): 315-325.

[12] Moonen, P., Bert B., Staf R., and Jan C., "Numerical modeling of the flow conditions in a closed-circuit low-speed wind tunnel", *Journal of Wind Engineering and Industrial Aerodynamics* 94, no. 10 (2006): 699-723.

[13] The Engineering Toolbox: Roughness and Surface Coefficients of Ventilation Ducts [Online] 2012.Available from: ⟨http://www.engineeringtoolbox.com⟩ (accessed 01.02.2012).

[14] Smith DA. Perturbation of vortex wakes for amelioration of the vortex wake hazard (Doctoral dissertation, 2003, Imperial College London (University of London)).

[15] Butt U, Egbers C. Aerodynamic characteristics of flow over circular cylinders with patterned surface. International Journal of Materials, Mechanics and Manufacturing. 2013 May; 1(2):121-25.

[16] SARIOĞLU M, Yavuz T. Vortex shedding from circular and rectangular cylinders placed horizontally in a turbulent flow. Turkish Journal of Engineering and Environmental Sciences. 2000 Sep 6; 24(4):217-28.

[17] Azzawi, I. D. J., Jaworski, A. J., and Mao, X. (December 4, 2020). "An Overview of Synthetic Jet Under Different Clamping and Amplitude Modulation Techniques." ASME. *J. Fluids Eng*. March 2021; 143(3): 031501. https://doi.org/10.1115/1.4048930

 doi:10.20944/preprints202208.0361.v1

[18] Chong T., Joseph P., Davies P. Design and Characterisation of a Quiet, Low Turbulence Open Jet Blow Down Wind Tunnel in ISVR, ISVR Technical Report No. 322 University of Southampton, 2008.